

Use of slow sound to design perfect and broadband passive sound absorbing materials

J.-P. Groby,^{a)} R. Pommier, and Y. Aurégan

Laboratoire d'Acoustique de l'Université du Maine (LAUM), Unité Mixte de Recherche 6613 Centre National de la Recherche Scientifique, Avenue O. Messiaen, 72085 Le Mans, France

(Received 17 July 2015; revised 21 March 2016; accepted 21 March 2016; published online 6 April 2016)

Perfect (100%) absorption by thin structures consisting of a periodic arrangement of rectangular quarter-wavelength channels with side detuned quarter-wavelength resonators is demonstrated. The thickness of these structures is 13–17 times thinner than the acoustic wavelength. This low frequency absorption is due to a slow sound wave propagating in the main rectangular channel. A theoretical model is proposed to predict the complex wavenumber in this channel. It is shown that the speed of sound in the channel is much lower than in the air, almost independent of the frequency in the low frequency range, and it is dispersive inside the induced transparency band which is observed. The perfect absorption condition is found to be caused by a critical coupling between the rectangular channel (sub-wavelength resonators) and the incoming wave. It is shown that the width of a large absorption peak in the frequency spectrum can be broadened if several rectangular channels in the unit cell are detuned. The detuning is achieved by varying the length of the side resonators for each channel. The predicted absorption coefficients are validated experimentally. Two resonant cells were produced with stereolithography which enabled the authors to incorporate curved side resonators. © 2016 Acoustical Society of America.

[<http://dx.doi.org/10.1121/1.4945101>]

[KVH]

Pages: 1660–1671

I. INTRODUCTION

A perfect absorber, i.e., a structure which absorbs 100% of the incident acoustic energy, of very small thickness is of great scientific and engineering interest. Until now, porous or fibrous materials¹ have been the common choice for noise passive control due to their ability to dissipate sound through thermal and viscous losses. This results in limitations: to absorb low frequency sound, bulky and heavy treatments are required even when optimized multilayer or graded materials² are used. Acoustic absorption can also be performed by means of micro-perforated panels^{3,4} with tuned cavity depth behind the panels. A large review of the existing acoustic absorbing structures can be found in Ref. 5. To overcome imperfect impedance matching to the incoming wave on structures with dimensions comparable to the wavelength, several strategies have been followed these last decades usually consisting in coupling porous materials with resonant features, double porosity materials,⁶ metaporous materials,^{7–10} dead-end porosity materials,^{11,12} or in coupling purely resonant components, membranes,^{13–15} Helmholtz resonators,^{15,16} or quarter-wavelength resonators (QWRs) making use of slow sound.^{12,17}

In these last types of passive absorption systems the balance between the rate of energy leakage and the inherent losses of the resonators is of fundamental relevance for their reflection properties.^{15,18} When these are well balanced, the critical coupling condition is fulfilled, leading to an impedance matching and maximum absorption at the resonance frequency. In the present article, we critically couple periodic

QWRs loaded by detuned QWRs to lower their resonance frequencies making use of the slow sound propagation together with the inherent attenuation. In acoustics, most of the theoretical and experimental evidences of slow sound have been achieved by considering sound propagation (i) in pipes with a series of detuned resonators (mostly Helmholtz resonators) separated by a subwavelength distance creating an induced transparency band (ITB),¹⁹ or with a series of tuned or detuned resonators separated by half of the wavelength giving rise to a coupling between the resonators and the Bragg bandgap,²⁰ (ii) in waveguided sonic crystals;²¹ or (iii) in lined ducts.²² So far, only a few studies have been focusing on the dissipation (dispersion and attenuation) of slow sound propagation,²³ even if dissipation has been sometimes noticed or discussed^{19,20,24} and only a few studies make use of the slow sound together with its attenuation to design a sub-wavelength acoustic absorber in two dimensions.¹⁷

A periodic structure whose unit cell consists of unique QWR of rectangular cross-section, named pore in the following, loaded by detuned QWRs is first critically coupled. The main advantage of this subwavelength resonator when compared to a usual Helmholtz one is a relatively large aperture enabling easy tuning of the resistivity of the structure. To some extent, it acts similarly as tapered labyrinthine acoustic metamaterials.²⁵ In a second step, a periodic structure whose unit cell consists in several pores of rectangular cross-section also loaded by different detuned QWRs are critically coupled. This pore differs from the length of the side resonators. Perfect absorption can be achieved over a large frequency band for wavelength again much larger than the usual 4 times the depth of the structure limit. Absorption in

^{a)}Electronic mail: Jean-Philippe.Groby@univ-lemans.fr

diffuse field is also investigated. Absorption at higher frequencies is also large in this configuration thanks to the coupling between the higher order resonances of the pores and ITBs of each pore avoiding the bandgap. The effective parameters enabling the description of the structure behavior are derived. It is shown that detuning enables to open the ITB. Slow sound propagation is demonstrated and equations of the speed of sound are derived. The speed of sound possesses a plateau at low frequency and is necessarily dispersive inside the ITB.¹⁹ Finally, experimental validations are performed at normal incidence on samples with curved loading QWRs produced by stereolithography showing good agreement with the calculations.

II. DESCRIPTION OF THE CONFIGURATION

A unit cell of the three-dimensional (3D) scattering problem together with a sketch of a loaded rectangular pore are shown in Figs. 1(a) and 1(b). Before the addition of the loading QWRs, the unit cell is composed of N rectangular cross-section straight pores. The n th pore of section $w_1^{(n)} \times w_2^{(n)}$ and height $L^{(n)}$ is occupied by a material $M^{p(n)}$, whose parameters account for both the viscous and thermal losses at each lateral boundary and are recalled in Appendix A. The total thickness of the structure is $L = \max_{n \in N}(L^{(n)})$. The upper and lower flat and mutually parallel boundaries of the structure, whose x_3 coordinates are L and $L - L^{(n)}$, are designated by Γ_L and $\Gamma_0^{(n)}$, respectively. The thermal (and viscous) losses are neglected on these two boundaries and a Neumann type boundary condition is applied on them, i.e., the normal velocity vanishes on Γ_L and $\Gamma_0^{(n)}$. The corner of the n th tube is located at $x_1 = d_1^{(n)}$ and $x_2 = d_2^{(n)}$, which both refer to the boundary on which a Neumann type boundary condition is applied, i.e., the interface $\Gamma_N^{(n)}$, or to the lower left corner in case of loading on two opposite sides of the pore. The upper semi-infinite material M^a , i.e., the ambient fluid that occupies Ω^a , and $M^{p(n)}$ are in firm contact at the boundaries $\Gamma_{ap}^{(n)}$, $\forall n \in \mathcal{N}$, i.e., the pressure and normal velocity are continuous across $\Gamma_{ap}^{(n)}$.

A periodic set of QWRs ($r_n^{(n)}$ in radii and $l_n^{(n)}$ in length tubes) are plugged on the pore lateral sides of inner normal \mathbf{n} , i.e., $\mathbf{n} = \pm 1$ if the tubes are plugged along the positive or

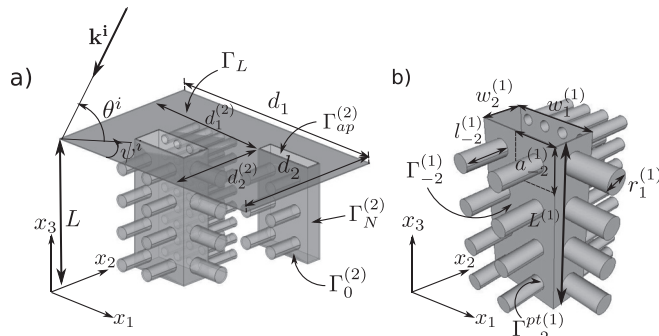


FIG. 1. (a) Example of a $d_1 \times d_2$ -periodic structure, whose unit cell is composed of two rectangular pores and (b) sketch of a loaded rectangular pore by a periodic set of QWRs of circular cross-section.

negative x_1 axis or $\mathbf{n} = \pm 2$ if the tubes are plugged along the positive or negative x_2 axis. These QWRs are arranged with a square lattice of size $a_n^{(n)}$. The material $M_n^{t(n)}$ that occupies each tube $\Omega_n^{t(n)}$ is modeled as a circular tube where both the viscous and thermal losses are accounted for, see Appendix A. This material is in firm contact with $M^{p(n)}$ through $\Gamma_n^{pt(n)}$, i.e., the pressure and normal velocity are continuous across $\Gamma_n^{pt(n)}$. The thermal losses are neglected at the surfaces ending each tube and a Neumann type boundary condition is applied on these boundaries. The conditions on $\Gamma_n^{pt(n)}$ also reduce to an impedance one applied on the whole interface $\Gamma_n^{(n)}$ in the following, because the considered wavelengths are much larger than the dimensions of $\Gamma_n^{pt(n)}$ and the periodicity of this arrangement $a_n^{(n)}$. This impedance classically reads as $Z_n^{(n)} = \pm i Z_n^{t(n)} \cotan(k_n^{t(n)} l_n^{(n)}) / \phi_n^{t(n)}$, wherein $Z_n^{t(n)} = \sqrt{\rho_n^{t(n)} K_n^{t(n)}}$ is the impedance of $M_n^{t(n)}$, $k_n^{t(n)}$ is the wavenumber inside the tube, $\phi_n^{t(n)}$ is the ratio between the area of $\Gamma_n^{pt(n)}$ over one of the unit cells, i.e., a surface porosity $\phi_n^{t(n)} = \pi(r_n^{(n)})^2 / (a_n^{(n)})^2$. The sign \pm depends on whether the resonators are plugged on the right/top (+ sign) or left/bottom (- sign) side of the pore. In what follows, only the positive sign will be used and

$$Z_n^{(n)} = i Z_n^{t(n)} \cotan(k_n^{t(n)} l_n^{(n)}) / \phi_n^{t(n)}. \quad (1)$$

Note that the use of an impedance condition is suitable in the presence of a series of side resonators along the main pore. Therefore, a single pair of side detuned resonators can hardly be modeled through an impedance condition.²⁶

The incident wave propagates in Ω^a and is expressed by $p^i(\mathbf{x}) = A^i e^{i(k_1^i x_1 + k_2^i x_2 - k_3^i (x_3 - L))}$, wherein $k_1^i = -k^a \cos \theta^i \sin \phi^i$, $k_2^i = k^a \cos \theta^i \cos \phi^i$, with θ^i the elevation and ϕ^i the azimuth, and $A^i = A^i(\omega)$ is the signal spectrum.

In each domain Ω^α ($\alpha = a, p^{(n)}, t^{(n)}$), the pressure field fulfills the Helmholtz equation

$$\nabla \cdot \left(\frac{1}{\rho^\alpha} \nabla p^\alpha \right) + \frac{(k^\alpha)^2}{\rho^\alpha} p^\alpha = 0, \quad (2)$$

with the density ρ^α and the wavenumber $k^\alpha = \omega/c^\alpha$, defined as the ratio between the angular frequency ω and the sound speed $c^\alpha = \sqrt{K^\alpha/\rho^\alpha}$.

As the problem is periodic and the excitation is due to a plane wave, each field (X) satisfies the Floquet-Bloch relation

$$X(\mathbf{x} + \mathbf{d}) = X(\mathbf{x}) e^{i k_1^i d}. \quad (3)$$

Consequently, it suffices to examine the field in the elementary cell of the material to get the fields, via the Floquet relation, in the other cells.

III. SOLUTION OF THE PROBLEM

A. Field representations

Separation of variables, radiation conditions, and Floquet theorem lead to the representations

$$p^a(\mathbf{x}) = \sum_{(q,g) \in \mathbb{Z}^2} [A^i e^{-ik_{3qg}^a(x_3-L)} \delta_{qg} + R_{qg} e^{ik_{3qg}^a(x_3-L)}] e^{ik_{1q}^a x_1 + ik_{2g}^a x_2}, \quad \forall \mathbf{x} \in \Omega^a, \quad (4)$$

wherein δ_{qg} is the Kronecker symbol, $k_{1q}^a = k_1^i + (2q\pi/d_1)$, $k_{2g}^a = k_2^i + (2g\pi/d_2)$, and $k_{3qg}^a = \sqrt{(k^a)^2 - (k_{1q}^a)^2 - (k_{2g}^a)^2}$, with $\text{Re}(k_{3qg}^a) \geq 0$ and $\text{Im}(k_{3qg}^a) \geq 0$. The reflection coefficient of the plane wave denoted by the subscripts q and g is R_{qg} .

According to Refs. 27 and 28, the pressure field $p^{(n)}$ admits the pseudo-modal representation, that already accounts for the boundary conditions on $\Gamma_0^{(n)}$, Γ_N , and $\Gamma_n^{(n)}$,

$$p^{(n)} = \sum_{(m,o) \in \mathbb{N}^2} A_{mo}^{(n)} \Phi_{1m}^{(n)}(x_1 - d_1^{(n)}) \Phi_{2o}^{(n)}(x_2 - d_2^{(n)}) \times \cos(k_{3mo}^{(n)}(x_3 + L^{(n)} - L)), \quad \forall \mathbf{x} \in \Omega^{(n)}, \quad (5)$$

wherein $A_{mo}^{(n)}$ are the coefficients of the pseudo-modal representation, $k_{3mo}^{(n)} = \sqrt{(k^{(n)})^2 - (k_{1m}^{(n)})^2 - (k_{2o}^{(n)})^2}$, with $\text{Re}(k_{3mo}^{(n)}) \geq 0$ and $\text{Im}(k_{3mo}^{(n)}) \geq 0$, and $\Phi_{1m}^{(n)}(x_1)$ and $\Phi_{2o}^{(n)}(x_2)$ are the mode in the x_1 and x_2 directions, respectively. The different modal expansion and mode dispersion relations are presented in Appendix B, depending on either the impedance condition is applied on any, one, or two opposite sides of the pore. For simplicity, we will consider the modal decomposition only in the x_1 direction. The modes $\Phi_{1m}^{(n)}(x_1)$ are either orthogonal or bi-orthogonal and the orthogonality relation reads as $\int_0^{w_1} \Phi_{1m}^{(n)}(x_1) \Phi_{1M}^{(n)}(x_1) dx_1 = \delta_{Mm} w_1^{(n)} N_{1m}^{(n)}$. In particular, the zero-order low frequency approximation $\tilde{k}_{10}^{(n)}$, arising from the condition $k_{10}^{(n)} w_1 \ll 1$, is

$$\tilde{k}_{10}^{(n)} = \frac{1}{w_1^{(n)}} \sqrt{\frac{-i\omega \rho^{p(n)} w_1^{(n)}}{Z_1^{(n)}}}, \quad (6)$$

when an impedance condition is applied on a single side and is

$$\tilde{k}_{10}^{(n)} = \frac{1}{w_1^{(n)}} \sqrt{\frac{-i\omega \rho^{p(n)} w_1^{(n)} (Z_1^{(n)} + Z_{-1}^{(n)} - i\omega \rho^{p(n)} w_1^{(n)})}{Z_1^{(n)} Z_{-1}^{(n)}}}, \quad (7)$$

when impedance conditions are applied on both sides of the pores.

B. The linear system for the solution of R_{qg}

The application of the boundary conditions on each interface $\Gamma_{ap}^{(n)}$ leads to two sets of coupled equations in terms of $A_{mo}^{(n)}$ and R_{qg} .

The combination of these two sets of equations leads to the solution either in terms of R_{qg} or in terms of $A_{mo}^{(n)}$, these two solutions being linked one with each other. In particular, the linear system of equations for the solution for R_{qg} , $\forall (q, g) \in \mathbb{Z}^2$, is

$$R_{qg} - \frac{i\rho^a}{k_{3qg}^a} \sum_{(Q,G) \in \mathbb{Z}^2} R_{QG} \sum_{n \in \mathcal{N}(m,o) \in \mathbb{Z}^2} \sum_{n \in \mathcal{N}(m,o) \in \mathbb{Z}^2} \frac{k_{3mo}^{(n)} \phi^{p(n)}}{N_{1m}^{(n)} N_{2o}^{(n)}} \times \tan(k_{3mo}^{(n)} L^{(n)}) I_{1mq}^{(n)-} I_{2og}^{(n)-} I_{1mQ}^{(n)+} I_{2oG}^{(n)+} = A^i \delta_{qg} + A^i \sum_{n \in \mathcal{N}(m,o) \in \mathbb{Z}^2} \sum_{n \in \mathcal{N}(m,o) \in \mathbb{Z}^2} \frac{i\rho^a k_{3mo}^{(n)} \phi^{p(n)}}{k_{3qg}^a \rho^{p(n)} N_{1m}^{(n)} N_{2o}^{(n)}} \times \tan(k_{3mo}^{(n)} L^{(n)}) I_{1mq}^{(n)-} I_{2og}^{(n)-} I_{1mQ}^{(n)+} I_{2oG}^{(n)+}, \quad (8)$$

where $\phi^{p(n)} = w_1^{(n)} w_2^{(n)} / d_1 d_2$ is the surface porosity of the n th pore, such that $\cup_{n \in \mathcal{N}} \phi^{p(n)} = \phi^p$ is the global surface porosity of the structure, and $I_{mq}^{(n)\pm}$ depicts the aperture of the pore on the semi-infinite half space through $\Gamma_{ap}^{(n)}$. The expressions of $I_{mq}^{(n)\pm}$ are given in Appendix C.

The system [Eq. (8)] is solved for each (q, g) pair. The absorption coefficient A is then calculated through

$$A = 1 - \sum_{(qg) \in \mathbb{Z}^2} \frac{\text{Re}(k_{3qg}^a)}{k_{300}^a} \|R_{qg}\|^2. \quad (9)$$

The dimensions of the studied configurations are given in Table I.

IV. ANALYSIS OF THE DISPERSION RELATION IN A PORE

For simplicity, the superscript p refers to the pore, while the exponent l refers to the QWR. In Ref. 17, the dispersion relation [Eq. (B1)] was analyzed showing that the low frequency solution [Eq. (6)] could be used as a first approximation and exhibits a combined effect of a large decrease of the sound speed together with an increase of the attenuation in a slit of width w_1 with the ratio $\phi^l l / w_1$. Following this idea and considering one straight pore of cross section $w_1 \times w_2$ loaded by two sets of identical QWRs, two cases should be analyzed: when the impedances are applied on two adjacent sides of the pore (case 1) and when they are applied on two opposite sides of the pore, for example, along the x_1 axis (case 2). At low frequency ($k^l l \ll 1$), the speed of sound in the pore, $c = \omega / \tilde{k}_3^p$, reads as $c = c^p / \sqrt{1 + (Z^p c^p \phi^l l / Z^l c^l)(1/w_1 + 1/w_2)}$ for case 1 and as $c = c^p / \sqrt{1 + (2Z^p c^p \phi^l l / Z^l c^l w_1)}$ for case 2. In this last case, the last term of the numerator of Eq. (7), which traduces the coupling between the two sets of QWRs, vanishes because it is of second order in terms of $k^l l$ and therefore does not influence the speed of sound at low frequency. No coupling can be noticed at low frequency. The formulas only differ from the dependence in terms of w_2 . In case 1, both w_1 and w_2 are constrained by the presence of the QWRs, i.e., $w_1 \geq a$ and $w_2 \geq a$, while in case 2 w_1 can be very small, allowing the speed of sound to be very small and increasing the attenuation, $\text{Im}(\tilde{k}_3^p) = \text{Im}(k^p \sqrt{1 + (2Z^p c^p \phi^l l / Z^l c^l w_1)})$. This last case also appears more efficient, and we will also focus on cases where the impedances are applied on opposite sides.

Let us now consider the detuned case when both sets of QWRs only differ from their length, i.e., l_1 and l_{-1} , and in particular, the dimension of configuration C1. Figures 2(a) and 2(b) depict, respectively, the real and imaginary part of k_3^p and the real part of c_3^p . Again, the low frequency solution

TABLE I. Dimension of the considered configurations (mm).

Conf.	L	$d_1 \times d_2$	$w_1^{(n)} \times w_2^{(n)}$	$d_1^{(n)} \times d_2^{(n)}$	l_1, l_{-1}	a	r
C1	30	84×42	1.5×20	$(24.5 \times 11); (58 \times 11)$	$(35, 24); (24, 35)$	5	1.75
C1, Eq. (12)	#	42×42	#	/	35, 24	#	#
C2	28	84×84	3.25×7	$(2.5 \times 7.65); (9.5 \times 13.4)$	$(50, 30); (43, 23)$	7	2.5
			#	(16.5×19.4)	$(35, 19)$	#	#
			#	$(74.5 \times 7.65); (67.5 \times 13.4)$	$(50, 30); (43, 23)$	#	#
			#	(60.5×19.4)	$(35, 19)$	#	#
			#	$(2.5 \times 73.1); (9.5 \times 67.35)$	$(30, 50); (23, 43)$	#	#
			#	(16.5×61.35)	$(19, 35)$	#	#
			#	$(74.5 \times 73.1); (67.5 \times 67.35)$	$(30, 50); (23, 43)$	#	#
			#	(60.5×61.35)	$(19, 35)$	#	#
C2, Eq. (12)	#	(42×42)	#	/	$(50, 30); (43, 23)$	#	#
			#	/	$(35, 19)$	#	#

[Eq. (7)] can be used as a good approximation of $k_{10}^{(n)}$. The slope of $\text{Re}(k_3^p)$ is smaller than the one of $\text{Re}(k^p)$ inside the passband, which again shows a decrease of the sound speed in the pore. At low frequency, the speed of sound reads as $c = c^p / \sqrt{1 + [Z^p c^p \phi^t (l_1 + l_{-1}) / Z^t c^t w_1]}$. This behavior is identical to the one of a configuration comprising a single set of QWR of length $l_{\text{tot}} = l_1 + l_{-1}$. The first advantage of using two sets of resonators instead of a single one is to shift the first bandgap, due to the quarter-wavelength resonance of the tubes, at a higher frequency, because obviously $c / 4l_{\text{tot}} < c / 4l_1$ and $c / 4l_{\text{tot}} < c / 4l_{-1}$. This allows propagation of waves at a small speed over a larger frequency band leading to possible large absorption. The second advantage lies in the detuning allowed by the balance of this total length on both sides of the pore leading to an ITB, Fig. 2(a). The bandgap arises when $\text{Re}(\tilde{k}_{10}) > \text{Re}(k^p)$ at first approximation. Around the resonances of the two sets of resonators $\tan(k^t l_j) \approx -1 / (k^t l_j - \pi/2)$, $j = \pm 1$. The frequencies for which $\text{Re}(\tilde{k}_3^p) = 0$ satisfies the equation $\text{Re}\{k^t + (Z^p c^p \phi^t / Z^t c^t w_1) [\pi - k^t (l_1 + l_{-1}) - k^t w_1 \phi^t \rho^p / \rho^t] / (k^t l_1 - \pi/2)(k^t l_{-1} - \pi/2)\} = 0$. This equation clearly exhibits the two resonances of the QWRs and a third frequency coupling the resonators. The low frequency bounds of both bandgaps are $f_l^{(1)} \approx 2400$ Hz and $f_l^{(2)} \approx 3500$ Hz and correspond to the QWRs resonance, while the higher frequency bound of the first bandgap is $f_h^{(1)} \approx 2800$ Hz. The higher bound of the second bandgap can be found through the approximation $\tan(k^t l_j) \approx k^t l_j - \pi$, $j = \pm 1$. This clearly shows that the ITB is due to the interaction of the first resonances of both

resonators. In absence of losses, it can be shown that k_{10} goes to infinity at the first resonance, while the higher order modes k_{1n} , $n > 1$ shift down of a value of π/w_1 . Similarly, at the second resonance, k_{11} goes to infinity, while the higher order modes k_{1n} , $n > 2$ again shift down of a value of π/w_1 . When losses are accounted for, and for a small value of $k_{1n} w_1$, these modes do not intersect anymore and a single continuous function \tilde{k}_{10} is found. The speed of sound reads as

$$c = c^p / \sqrt{1 + \frac{Z^p c^p \phi^t}{Z^t c^t w_1} \left(\frac{\pi/k^t - (l_1 + l_{-1}) - w_1 \phi^t \rho^p / \rho^t}{(k^t l_1 - \pi/2)(k^t l_{-1} - \pi/2)} \right)}$$

inside the ITB, where the last term of the numerator traduces the coupling between the two resonators. An important remark is that while the speed of sound possesses a plateau at low frequency, where the velocity is not dispersive, the speed of sound inside the ITB is necessarily dispersive and accounts for the coupling between the detuned resonators.

V. DERIVATION OF THE EFFECTIVE PARAMETERS

Adopting the same type of analysis as in Ref. 17, i.e., assuming the unique propagation of the modes $m=0$ and $o=0$ in the pores, $k_1^{(n)} w_1^{(n)} \ll 1$ and $k_2^{(n)} w_2^{(n)} \ll 1$, and the dominance of the zeroth order terms in I_{0q}^\pm ensuring $I_{00}^+ I_{00}^- / N_0 \approx 1$, the system Eq. (8) reduces to the unique calculation of R_{00} , which takes the following form:

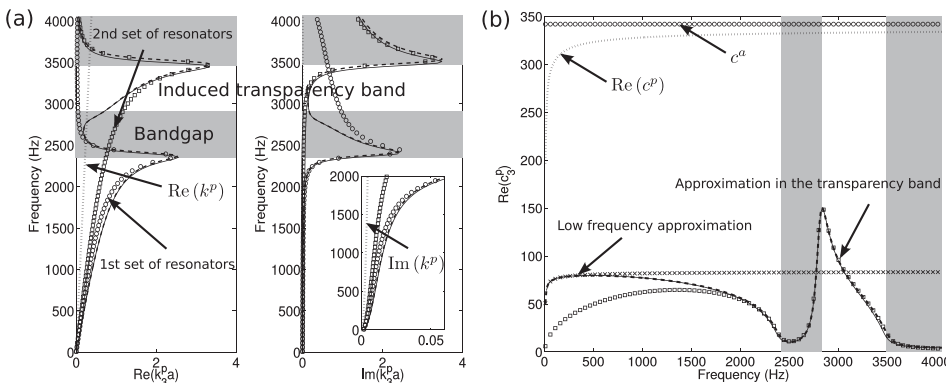


FIG. 2. Configuration 1. (a) Real and imaginary parts of k_3^p (solid line) and \tilde{k}_3^p (dashed line), both real and imaginary parts of k^p (dotted line) and of \tilde{k}_3^p (dashed line) when only the first (o) and the second (x) set of QWRs are present are also plotted. The inset shows a zoom at low frequency of the imaginary part. (b) Real part of c_3^p (solid line) and \tilde{c}_3^p (dashed line) together with its low frequency approximation (x) and its approximation inside the ITB (□). Real part of c^p (dotted line) and c^a (o) are also plotted.

$$R_{00} = A^i \frac{\frac{\sin \theta^i}{Z_0} + \sum_n^N \frac{i\phi^{p(n)} k_3^{(n)} \tan(k_3^{(n)} L^{(n)})}{\omega \rho^{(n)}}}{\frac{\sin \theta^i}{Z_0} - \sum_n^N \frac{i\phi^{p(n)} k_3^{(n)} \tan(k_3^{(n)} L^{(n)})}{\omega \rho^{(n)}}}. \quad (10)$$

It is very important to specify that the condition leading to the dominance of the zeroth order terms in I_{0q}^\pm is only attached to the arrangement of the pores in the unit cell. A simple identification with the classical formula of the reflection coefficient of a rigidly backed homogeneous slab leads to a surface admittance of each pore

$$Y_{\text{eff}}^{(n)} = \frac{-i\phi^{p(n)} k_3^{(n)} \tan(k_3^{(n)} L^{(n)})}{\omega \rho^{(n)}}, \quad (11)$$

which does not depend on the angle of incidence. Another identification leads to $Z_{\text{eff}}^{(n)} = \omega \rho^{(n)} / k_3^{(n)} \phi^{p(n)}$ and $k_{\text{eff}}^{(n)} = k_3^{(n)}$ for this locally reacting material,¹ considering each pore independently. Let us also consider only one straight pore per spatial period for simplicity.

Similar to what was done in Ref. 17, the total porosity of the pore $\phi_{\text{tot}} = \phi^p (1 + \phi^t (l_1 + l_{-1}) / w_1)$ should be introduced for these quantities to be consistent and in

$$\rho_{\text{eff}} = \left(1 + \frac{\phi^t (l_1 + l_{-1})}{w_1}\right) \frac{\rho^{(1)}}{\phi_{\text{tot}}}, \quad K_{\text{eff}} = \frac{K^p \left(1 + \frac{\phi^t (l_1 + l_{-1})}{w_1}\right)}{\phi_{\text{tot}} \left(1 + \frac{Z^p \phi^t}{w_1 Z^t k^p} \left(\tan(k^t l_1) + \tan(k^t l_{-1}) - \frac{\rho^p w_1 k^t \phi^t}{\rho^t} \tan(k^t l_1) \tan(k^t l_{-1})\right)\right)}. \quad (12)$$

At low frequency, when $k^t l_1 \ll 1$ and $k^t l_{-1} \ll 1$, the effective bulk modulus reduces to $K_{\text{eff}} = K^p [1 + (\phi^t (l_1 + l_{-1}) / w_1)] / \phi_{\text{tot}} [1 + (K^p \phi^t (l_1 + l_{-1}) / w_1 K^t)]$. Particularly noticeable is the comparison with the first order homogenization theory.²⁹⁻³¹ Classically, the homogenized bulk modulus K_{hom} and density ρ_{hom} are

$$\begin{aligned} \frac{1}{\rho_{\text{hom}}} &= \frac{\phi_{\text{tot}}}{\rho} = \frac{\phi^p}{\rho^{(1)}}, \\ \frac{1}{K_{\text{hom}}} &= \frac{\phi_{\text{tot}}}{K} = \frac{\phi^p}{K^p} + \frac{\phi^p (l_1 + l_{-1}) w_2}{K^t d_1 d_2} \\ &= \frac{\phi^p}{K^p} \left(1 + \frac{\phi^t K^p (l_1 + l_{-1})}{K^t w_1}\right), \end{aligned} \quad (13)$$

which fit the low frequency approximation of Eq. (12).

Figure 3 depicts the real [Fig 3(a)] and imaginary [Fig. 3(b)] part of both effective parameters normalized by ϕ_{tot} / P_0 for the bulk modulus and by $\phi_{\text{tot}} / \rho^a$ for the density. The bulk modulus is lower than in absence of the resonators while a large tortuosity-like effect is exhibited for the effective density. This tortuosity-like effect is responsible for the

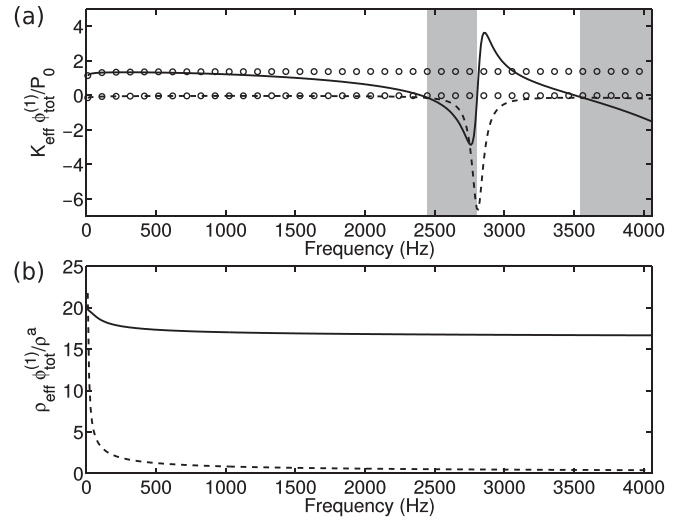


FIG. 3. Configuration 1. (a) Real (solid line) and imaginary (dashed line) of $K_{\text{eff}} \phi_{\text{tot}} / P_0$ and (b) real (solid line) and imaginary (dashed line) of $\rho_{\text{eff}} \phi_{\text{tot}} / \rho^a$. The low frequency approximation, which fit the classical homogenization theory, of $K_{\text{eff}} \phi_{\text{tot}} / P_0$ also plotted (o).

particular, for $\lim_{\omega \rightarrow 0} \phi_{\text{tot}} K_{\text{eff}} = P_0$. The effective density and bulk modulus, where the approximation [Eq. (7)] is made, reads as

low speed of sound encountered at the low frequency. It is closer to the concept of static tortuosity introduced in the Pride-Lafarge model¹ than the usual tortuosity which refers to high frequency behavior of regular porous materials. The expressions of the effective bulk modulus and density are valid below the first bandgap for the whole material, because of the arrangement of the pores and dispersion of \tilde{k}_{10} close to the bandgap as explained in Ref. 17, while still valid for what happens in the pore. In the latter, the effective bulk modulus is negative inside the bandgaps as noticed by several authors since the seminal publication.³² The classical homogenization result for $K_{\text{hom}} \phi_{\text{tot}} / P_0$ is also plotted and fits well the result below 750 Hz, i.e., far below the first bandgap.

Effective parameters of configurations involving several pores can be derived in a similar way, i.e., deriving the effective properties for each pore. Noticeable is the fact that the classical homogenization theory is not necessarily suitable; the scale separation between the pores being not always satisfied in the general case. Effectively, let us consider a unit cell composed of N pores loaded by QWRs oriented along the x_1 axis only differing from their length $l_1^{(n)}$ and $l_{-1}^{(n)}$. The homogenized density and bulk modulus are in this case

$$\begin{aligned} \frac{1}{\rho_{\text{hom}}} &= \frac{\phi_{\text{tot}}}{\rho} = \sum_{n=1}^N \frac{N\phi^{(n)}}{\rho^{(n)}} = \frac{N\phi^{(1)}}{\rho^{(1)}}, \\ \frac{1}{K_{\text{hom}}} &= \frac{\phi_{\text{tot}}}{K} = \sum_{n=1}^N \frac{\phi^{(n)}}{K^p} + \frac{\phi^{(n)}(l_1^n + l_{-1}^n)w_2}{K^t d_1 d_2} \\ &= N \frac{\phi^{(1)}}{K^p} \left(1 + \frac{\phi^t K^p}{K^t w_1} \sum_{n=1}^N \frac{(l_1^{(n)} + l_{-1}^{(n)})}{N} \right), \end{aligned} \quad (14)$$

which are the parameters of N identical pores loaded by the mean value of the resonators lengths $\sum_{n=1}^N (l_1^{(n)} + l_{-1}^{(n)})/N = \text{mean}(l_1^{(n)} + l_{-1}^{(n)})$. This can only lead to one absorption peak around the quarter-wavelength resonance of the pores which is different from what is expected, for example, in Sec. VI A. In other words, this representation is suitable only when all $\tan(k_3^{(n)}L^{(n)})$ are of the same order.

Noticeable is also the fact that more refine homogenization procedures such as the multi-scale asymptotic method⁹ or non-local theory³³ can be used to account for the resonant features of the present problem in the effective parameters.

VI. RESULTS AND DISCUSSION

A. One pore per spatial period and critical coupling analysis

We first focus on the absorption at normal incidence and low frequency, using the previously derived effective

parameters ρ_{eff} and K_{eff} , Eq. (12), for configuration 1. We note that these effective parameters derived for configuration 1 are those of half of the unit cell, because these parameters do not depend on the pore location and QWR orientations. The critical coupling analysis is performed by use of these parameters and not for the whole calculation because it avoids any problem related to the choice of the correct Riemann sheet. Effectively, the choice of the higher order mode in complex frequency analysis is usually not detailed in the literature. The acoustic response of the configuration can be analyzed as the coupling of resonators. The reflection coefficient takes the classical form $R_{00} = [iZ_{\text{eff}}\cotan(k_{\text{eff}}L) - Z_0] / [iZ_{\text{eff}}\cotan(k_{\text{eff}}L) + Z_0]$. In Ref. 34, the authors performed an analysis of $|R_{00}|^2$ in the complex frequency plan $\Omega = \omega + i\Omega_p$. Figure 4(a) depicts $\log |R_{00}|^2$ for configuration 1 showing that the viscous and thermal losses exactly compensate the radiation losses. In absence of losses, the first zero and pole of $|R_{00}|^2$ are symmetric with respect to the real frequency axis, zero in the upper half space and pole in the lower half space. The leakage does not exactly correspond to $Q_{\text{leak}} = \text{Im}(\Omega_p)/2\text{Re}(\Omega_p)$ where Ω_p is the complex frequency of the pole in the absence of dissipation, because Q_{leak}^{-1} is not small compared to 1 in this case. The introduction of losses induces a complex frequency map deformation. The first zero and pole become symmetric with respect to $\text{Im}(Z_{\text{eff}}\cotan(k_{\text{eff}}L)) = 0$, and therefore the former can be exactly located on the real frequency axis leading to a perfect absorption, Fig. 4(c). The

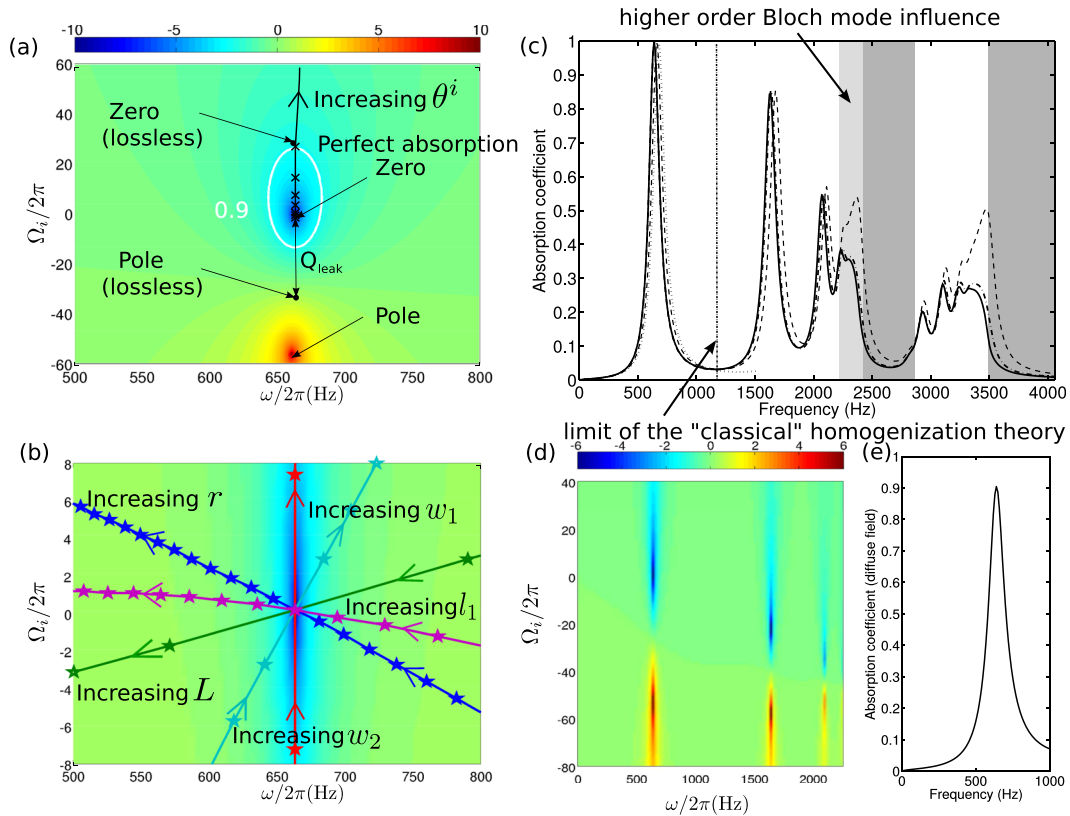


FIG. 4. (Color online) Configuration 1. (a) Map of $\log(|R_0|^2)$ in a function of Ω , the white line depicts the isovalue of an absorption coefficient of 0.9. The evolution of the zero position in function of θ^i is also plotted. (b) Zoom of the $\log(|R_0|^2)$ around the perfect absorption point and evolution of the zero position in function of r , w_1 , w_2 , l_1 , and L : the stars show the exact location in the parametric analysis. (c) Absorption coefficient calculated with the present method (solid line), calculated with the effective parameters derived in Sec. V without (dashed line) and with (dashed-dotted line) length correction, and calculated with the low frequency approximation of the effective parameters derived in Sec. V, i.e., with the classical homogenization theory (dotted line). (d) Map of $\log(|R_0|^2)$ in function of Ω when length correction is accounted for, and (e) diffuse field absorption coefficient calculated with length correction.

reflection coefficient vanishes for $f=663$ Hz. The perfect absorption obtained for this configuration is due to an impedance matching, so to interference phenomena and not to a mode excitation.

The main interest of this representation yields in the parametric analysis. The upper half space is forbidden because it corresponds to exponentially growing terms with increasing t . This is particularly true when the pole is located in this half space. Here we are interested in the effect of the localization of the zero in the complex frequency map on the reflection coefficient along the real axis. Figure 4(b) shows the evolution of the location of zero in the complex frequency map when the different dimensions of the structure vary: r varies in [1.4 mm, 2.35 mm] with a step of 0.05 mm, w_1 varies in [1.3 mm, 1.7 mm] with a step of 0.1 mm, w_2 varies in [1.5 cm, 2.5 cm] with a step of 5 mm, l_1 varies in [2 cm, 7 cm] with a step of 5 mm, and L varies in [2.5 cm, 4 cm] with a step of 5 mm. Some of these steps are constrained by a and obviously a variation of r induces a variation of ϕ^l . This parametric study is quite important despite the fact that some of the results are obvious, because it enables to determine which parameter to tune to locate the zero of $|R_{00}|^2$ on the real frequency axis allowing a perfect absorption condition. Of particular interest is the influence of w_2 which greatly influences the position of zero thanks to a modification of ϕ^p . Similarly, a modification of l_1 (L_{-1} leads to identical results) mainly influences the zero position along the real frequency, but poorly along the imaginary frequency. The zeros corresponding to the higher order resonances of the pore are located below the real frequency axis [Fig. 4(d)], and therefore cannot lead to perfect absorption, but to peaks of large absorption.

Figure 4(c) depicts the absorption coefficient at normal incidence calculated with the effective parameters, Eq. (12), and calculated with the whole procedure, Eq. (8). The absorption is perfect for the effective parameter calculation at 663 Hz and very close to unity for the full calculation at 645 Hz. This is due to the radiation by the pore, which would require a length correction l_{corr} in the effective parameters derivation. This correction length can be evaluated numerically by reconstructing an equivalent impedance \tilde{Z} from the reflection coefficient of the zeroth order Bloch mode (unique propagating mode over the frequency band considered) calculated with the whole model through

$$\tilde{Z} - iZ_{\text{eff}}\cotan(k_{\text{eff}}L) = -i\omega\frac{\rho_0}{\phi^p}l_{\text{corr}}. \quad (15)$$

It is therefore obviously frequency dependent and complex, but we considered the mean value of its real part at low frequency leading to $l_{\text{corr}}=1.2$ mm. This value corresponds neither to the one of a rectangular orifice in baffle nor to the one of a grid of slits.³⁵ Accounting for this correction length let both calculations matched over the frequency band be considered. The absorption is nearly total for the whole calculation. The classical homogenization theory provides satisfying results below 1200 Hz, which is higher than the one encountered for in Sec. V, but still lower than the first bandgap. Despite the fact that the homogenized parameters

are different from the effective ones as calculated in the present paper, they are still close to them until 1200 Hz. The structure exhibits a full absorption coefficient for wavelength in the air ≈ 17.7 times its thickness. Before the bandgap, the efficiency of the calculation performed with the effective parameters, without correction length, decreases because of the large influence of the higher order Bloch modes enabled by the dispersion of the modes inside the pores. This is usually accounted for through Drude layers,^{36,37} but we show here that a correctly chosen correction length leads to similar results. This implicitly means that in the present case, the Drude layers would only account for an added mass at the entrance of the main pores. The absorption inside the ITB reaches 0.3.

The evolution of the location of the first zero in the complex frequency plan in function of the angle of incidence θ^i is plotted [Fig. 4(a)]. The cross depicts the location of the zero for $\theta^i=[90^\circ, 80^\circ, 70^\circ, 60^\circ, 50^\circ, 40^\circ, 30^\circ, 20^\circ]$. The evolution of the position of the zero is almost vertical. The resonance frequency of the pore, i.e., a QWR, does not depend on the angle of incidence. A small shift at high frequency is noticed for near grazing incidence, which is due to the curvature of the complex frequency plan. The isovalue corresponding to an absorption of 0.9 is an ellipse with the semi-major axis along the imaginary frequency. While this implies that the absorption peak is relatively narrow in frequency, Fig. 4(c), it also implies that the absorption is relatively stable when the position of the zeros is shifted along the imaginary frequency, i.e., when θ^i decreases for example. In practice, the absorption peak is larger than 0.9 for $\theta^i > 30^\circ$, but rapidly decreases for smaller θ^i . This means that this configuration is relatively efficient for diffuse field excitation. The diffuse field absorption as calculated through $\int_0^{\pi/2} (1 - \|R_{00}(\theta)\|^2) \cos\theta \sin\theta d\theta / \int_0^{\pi/2} \cos\theta \sin\theta d\theta$,¹ is depicted in Fig. 4(e), showing an absorption in diffuse field higher than 0.9 at 643 Hz. Note that the first Wood anomaly arises around 2000 Hz at grazing incidence and so does not contribute around the first absorption peak. We will now focus on the normal incidence.

B. Various pores per spatial period and critical coupling analysis

Different coupling between the pores exists: either leading to a single peak whose frequency width is broadened when the resonance frequencies are close enough, or leading to N peaks which can overlap. The first solution enables a perfect absorption from the coupling between pores which does not lead to perfect absorption independently. This particularly enables to consider the coupling of pores of small porosity $\phi^{p(n)}$, due to a very small width enabling low frequency absorption. Nevertheless, the large absorption frequency band is still narrow in this case, but the parameters resulting from the classical homogenization theory, Eq. (14), can be used. The second possibility widens the large absorption frequency band with N perfect absorption peaks. Another design strategy could consist in tuning the different pore contributions for the absorption to be large or perfect at various angles of incidence. Effectively, Eq. (16) clearly

exhibits a dependence on the angle of incidences. While the absorption peak frequency due to the resonance of each pore is not dependent from the angle of incidence, its amplitude is. Designing the pores for one to take over another one at various angles of incidence is doable. We follow the second possibility, focusing on the normal incidence.

Based on the conclusion of Sec. VIA, a unit cell with three pores has been designed using effective parameters in order to broaden the large absorption band by varying the lengths of the loading QWRs. The effective parameters derived for configuration 2 are those of a quarter of the unit cell, see Table I. The reflection coefficient takes the form of Eq. (10). If the resonance frequencies of the pores are close, it suggests to let the numerator of $|R_{00}|^2$ vanish, which will result in the critical coupling condition to be satisfied. In other words it suggests to minimize the following quantity over a specific frequency band:

$$\left| \frac{\sin \theta^i}{Z_0} - \sum_n \frac{i\phi^{(n)}k_3^{(n)} \left(k_3^{(n)}L^{(n)} - \frac{\pi}{2} \right)}{\omega\rho^{(n)}} \right|^2. \quad (16)$$

Doing so at low frequency leads to an optimal configuration exhibiting perfect absorption peaks with identical length resonators loading each pore. Effectively, the main differences of loading a pore with different length resonators happen at a higher frequency, Sec. IV, around the bandgaps and in the ITB, which is absent in the case of identical QWRs. We also adopted a similar technique as for Sec. VIA. The correction length of each pore has been determined independently through the formula used in Sec. VIA. These correction lengths are almost identical, therefore we used $l_{\text{corr}} = 1.9 \text{ mm}$ for each pore.

Figure 5(a) depicts $\log(|R_{00}|^2)$ in the complex frequency plan for configuration C2. The three zeros of $|R_{00}|^2$ are almost aligned on the real frequency axis, proving critical coupling for different frequencies. This time the deformation of the complex frequency map is performed through the equation $\sum_n \text{Im}(Z_{\text{eff}}^{(n)} \tan(k_{\text{eff}}^{(n)}L)) = 0$. A similar

parametric analysis was performed, showing the interdependence of each parameter, i.e., the coupling between the pores. For clarity of the presentation, this parametric study is not depicted here, the conclusion being more difficult to draw. The absorption coefficient of configuration C2 is depicted in Fig. 5(b). Again the perfect absorption peaks for the whole calculation are encountered for frequencies which are lower than those obtained with calculations run with the equivalent parameters without correction lengths accounted for. Of particular interest is that the absorption coefficient is larger than 0.7 for frequency in [760 Hz; 990 Hz] and perfect for 790, 870, and 960 Hz. The first perfect absorption frequency corresponds to a wavelength in the air 15 times larger than the sample thickness, while the third perfect absorption frequency corresponds to a wavelength in the air 13 times larger than the structure thickness. This time the absorption is larger than 0.9 for angle of incidence $\theta^i > 20^\circ$, but the three peaks collapse into two for $\theta^i < 40^\circ$ because of the coupling which is performed through interferences.

The frequency band over which the absorption is larger than 0.7 for configuration 1 is [609 Hz; 680 Hz]. Defining an indicator as being $q = \Delta f / f_{\text{mean}}$, where Δf is the frequency range and f_{mean} is the central frequency of this frequency range, we find $q = 0.1$ for configuration 1 and $q = 0.2$ for configuration 2, which means that configuration 2 provides, on average, twice more absorption than the first one using this criteria. Another particular interest of this configuration is that no bandgap is noticed anymore at high frequency. This is due to the interference of the higher resonances of the pores and of the waves within in the ITB.

VII. EXPERIMENTAL VALIDATION

Two epoxy resin (Accura 60) samples $4.2 \text{ cm} \times 4.2 \text{ cm}$ were produced by stereolithography. The loading resonators were curved in order for them to fit in the unit cell. It is important to note that the total length for configuration 1 for example, $l_1 + w_1 + L_{-1} = 6.05 \text{ cm}$ is larger than the diagonal of the elementary cell $42 \times \sqrt{2} \approx 5.94 \text{ cm}$. It is even worse for configuration 2 where the maximum length reaches $l_1 + w_1 + L_{-1} = 8.325 \text{ cm}$.

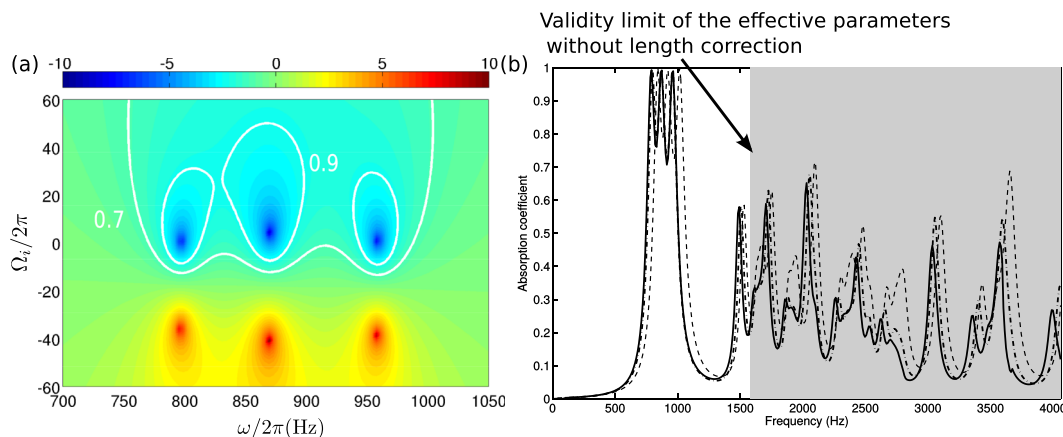


FIG. 5. (Color online) Configuration 2. (a) Map of $\log(|R_{00}|^2)$ in function of Ω (the two white curves depict the absorption contours for, respectively, 0.7 and 0.9) and (b) absorption coefficient calculated with the present method (solid line) and calculated with the effective parameters derived in Sec. V without (dashed line) and with (dashed-dotted line) correction length.

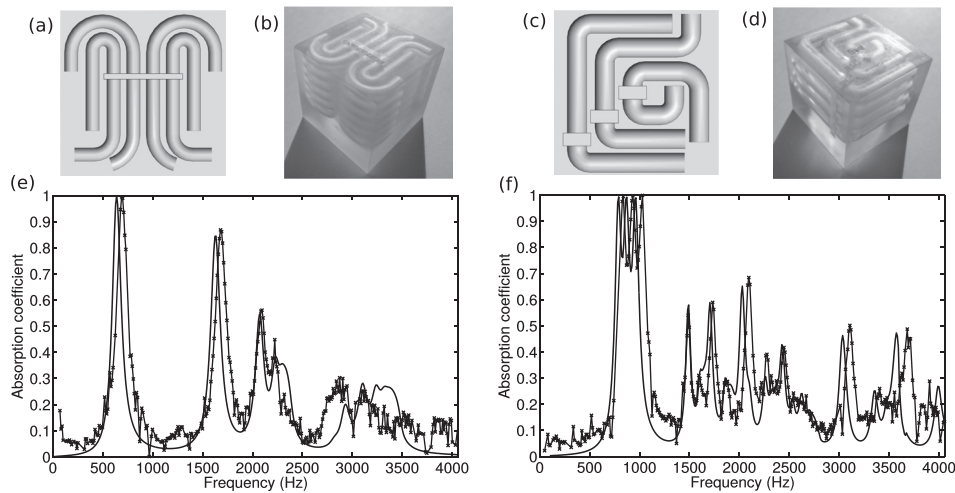


FIG. 6. Frontal section along the resonator diameter cut plane of samples 1 (a) and 2 (c), pictures of samples 1 (b) and 2 (d), and absorption coefficient measured (solid line with crosses) and simulated with the full model (solid line) of samples 1 (e) and 2 (f).

In Ref. 38, simple quarter-wavelength (and Helmholtz) resonators were already produced in a spiral showing correct agreement with the calculations. Figures 6(a) and 6(c) depict a frontal section along the QWR diameter cut plane of sample 1 and 2. This pattern is repeated 6 times for samples 1 and 4 times for sample 2 along the x_3 axis leading to a 3 cm thick pore sample 1 and a 2.8 cm thick pore sample 2. The bottom of the pore is also included in both samples.

The absorption coefficient of the samples is measured in an impedance tube with a square cross section $4.2\text{ cm} \times 4.2\text{ cm}$. The tube cutoff frequency is 4200 Hz. By assuming that plane waves propagate below the cutoff frequency, the infinitely rigid boundary conditions of the tube act like perfect mirrors and create a periodicity pattern in the x_1 and x_2 directions. Samples 1 and 2 are placed in the end of the tube against a copper plug that closes the tube and acts as a rigid boundary, therefore creating a periodicity along the x_1 and x_2 directions of, respectively, 8.4 and 4.2 cm for sample 1 and of, respectively, 8.4 and 8.4 cm for sample 2. This technique was previously used in various articles^{8,17,39} and allows to determine experimentally the absorption coefficient at normal incidence of a quasi-infinite two-dimensional or 3D periodic structure just with half or a quarter of the unit cell.

Figures 6(e) and 6(f) depict the experimental absorption coefficients of samples 1 and 2 and the calculated ones. The discrepancies, in particular, the shift at high frequency of the absorption peaks between the experiments and the calculation, are due to imperfections in manufacturing. Effectively, stereolithography consists in solidifying the liquid resin thanks to a laser. The remaining liquid resin is then removed by use of a solvent. Because of the complicated shape of the samples it was found almost impossible to remove the remaining resin from the bottom loading QWRs resulting in discrepancies in the QWR lengths, which are randomly distributed. In particular, some resonators in the bottom of the sample, where it is the most difficult to remove the resin, are obstructed at half of their lengths. This increases the speed of the waves traveling in the pore leading to a shift of the perfect absorption peak at higher frequencies. Another discrepancy arises from the location of the bandgap and ITB, which are both shifted at low

frequency. This suggests that the longest loading QWRs are longer than they should be. Their lengths were determined by equaling the neutral fiber of the curved resonators with the expected length. This result suggests that the correct way of designing them is not to consider the neutral fiber length but the longest curve of the resonators. Moreover, even if the curved resonators were drawn taking care of the curvatures, some of them exhibit very large ones, almost $\pi/2$. Nevertheless, the experimental curves are in good agreement with the calculations, particularly exhibiting broadband perfect absorption and large absorption in the transparency band for wavelength impinging the structure much larger than 4 times its thickness.

VIII. CONCLUSION

The acoustic properties of a sound absorbing structure consisting in a periodic arrangement of rectangular cross-section pores loaded by detuned QWRs are analyzed. In case of only one pore spatial period, the loading by two sets of QWRs on the opposite lateral faces was found preferable because it enables us (1) to consider smaller section dimension of the pore lowering very efficiently the speed of sound, (2) to shift the first bandgap, in which no absorption can be achieved, to the higher frequency when compared to a configuration with only one set of QWRs, and (3) to reduce the frequency width of the first bandgap by opening an ITB arising from the coupling of the two sets of QWRs. It was shown that the speed of sound possesses a plateau at low frequency whose value is much smaller than the speed of sound in the air. The speed of sound inside the ITB is also much smaller than the speed of sound in the air but is necessarily dispersive. It was shown that these pores are critically coupled to the incoming wave leading to perfect absorption for a wavelength in the air 17 times larger than the structure thickness. The complex frequency analysis, enabling the determination of the critical coupling condition, showed that while the large absorption frequency band is relatively narrow, its amplitude is stable for various angles of incidence, with an absorption peak larger than

0.9 for the angle of incidence in the range of $[90^\circ; 30^\circ]$. This offers interesting properties to explore in diffuse field perfect absorbers. The case of a unit cell consisting in three pores differing in terms of the lengths of the loading QWRs was then analyzed. The different types of coupling were discussed and the critical coupling condition was found to be more difficult to realize a broadband perfect absorption. Still, the configuration exhibits a broadband large absorption, with 3 perfect absorption peaks, for wavelength in the air 13 to 15 times the thickness of the structure. The pertinence of this structure to maintain a large absorption over the same frequency band was analyzed for various angles of incidence. Absorption at higher frequency can be large due to interferences of higher order quarter-wavelength resonances and waves arising from the ITB. These two configurations were then validated experimentally. The two samples were manufactured by stereolithography. The loading resonators were curved in order to fit in the unit cell. It was shown that the experimental data agreed with the model and exhibited perfect absorption for wavelength 17 times larger than the thickness of the first structure and between 13 to 15 times larger than the thickness of the second structure. Stereolithography was not necessarily

the most adequate rapid manufacturing technique to manufacture such material because (1) it is difficult to remove entirely the photosensitive liquid resin from the bottom loading resonators and (2) the correct length of the corresponding straight resonators is probably larger than the length of the neutral axis. These results offer quite interesting perspectives in terms of the design of perfect, broadband, and incident angular independent more complex sound absorbing structures, involving resonators of different natures.

ACKNOWLEDGMENTS

This work was partly supported by the ANR Project METAUDIBLE No. ANR-13-BS09-0003 co-funded by ANR and FRAE. The authors would like to thank V. Romero-Garcia for useful discussions on this work.

APPENDIX A: MATERIAL PARAMETERS IN STRAIGHT RECTANGULAR AND STRAIGHT CIRCULAR TUBES

When only plane wave propagates in a rectangular tube of section $w_1 \times w_2$, the equivalent complex and frequency dependent bulk modulus and density are⁴⁰

$$K^p = \frac{\gamma P_0}{\gamma + \frac{4i\text{Pr}\rho^a\omega(\gamma-1)}{\eta(w_1/2)^2(w_2/2)^2} \sum_{k \in \mathbb{N}} \sum_{m \in \mathbb{N}} \left(\alpha_k^2 \beta_m^2 (\alpha_k^2 + \beta_m^2) - \frac{i\text{Pr}\omega\rho^a}{\eta} \right)^{-1}}, \quad \rho^p = \frac{-\eta(w_1/2)^2(w_2/2)^2}{4i\omega \sum_{k \in \mathbb{N}} \sum_{m \in \mathbb{N}} \left(\alpha_k^2 \beta_m^2 (\alpha_k^2 + \beta_m^2) - \frac{i\omega\rho^a}{\eta} \right)^{-1}}, \quad (\text{A1})$$

wherein γ is the specific heat ratio, P_0 is the atmospheric pressure, Pr is the Prandtl number, η is the dynamic viscosity, and ρ^a is the air density, and $\alpha_k = 2(k + 1/2)\pi/w_1$ and $\beta_m = 2(m + 1/2)\pi/w_2$.

When only a plane wave propagates in a circular tube of radius r , the equivalent complex and frequency dependent bulk modulus and density are

$$K^t = \frac{\gamma P_0}{1 + 2(\gamma-1)/\sqrt{i\rho^a\text{Pr}\omega/\eta} J_1\left(r\sqrt{i\rho^a\text{Pr}\omega/\eta}\right)/rJ_0\left(r\sqrt{i\rho^a\text{Pr}\omega/\eta}\right)}, \quad \rho^t = \frac{\rho^a}{1 - 2/\sqrt{i\rho^a\omega/\eta} J_1\left(r\sqrt{i\rho^a\omega/\eta}\right)/rJ_0\left(r\sqrt{i\rho^a\omega/\eta}\right)}, \quad (\text{A2})$$

wherein J_n is the Bessel function of n th order.

APPENDIX B: MODAL REPRESENTATION IN A PORE AND DISPERSION RELATIONS

When both opposite surfaces of the pore are rigid, $\Phi_{1m}^{(n)}(x_1) = \cos(k_{1m}^{(n)}x_1)$ and $k_{1m}^{(n)} = m\pi/w_1^{(n)}$. These modes are said orthogonal and the orthogonality relation classically reads as $\int_0^{w_1} \Phi_{1m}^{(n)}(x_1)\Phi_{1M}^{(n)}(x_1)dx_1 = \delta_{Mm}w_1^{(n)}/\epsilon_m$, with $\epsilon_0 = 1$ and $\epsilon_m = 2$ for $m > 1$.

When one surface is rigid and on the other an impedance condition is applied, $\Phi_{1m}^{(n)}(x_1) = \cos(k_{1m}^{(n)}x_1)$ and $k_{1m}^{(n)}$ stratifies the dispersion relation

$$k_{1m}^{(n)} \tan\left(k_{1m}^{(n)}w_1^{(n)}\right) = \frac{-i\omega\rho^{p(n)}}{Z_1^{(n)}}. \quad (\text{B1})$$

This last equation is solved by use of a Muller's algorithm initiated with the low frequency approximations, $k_{1m}^{(n)}w_1^{(n)} \ll 1$.¹⁷ These modes are said to be bi-orthogonal and the bi-orthogonality relation reads as²⁷

$$\int_0^{w_1} \Phi_{1m}^{(n)}(x_1)\Phi_{1M}^{(n)}(x_1)dx_1 = \frac{\delta_{Mm}w_1^{(n)}}{2} \left(1 + \text{sinc}\left(2k_{1m}^{(n)}w_1^{(n)}\right)\right) = \delta_{Mm}w_1^{(n)}N_{1m}^{(n)}. \quad (\text{B2})$$

Finally, when impedance conditions are applied on both surfaces, $\Phi_{1m}^{(n)}(x_1) = \sin(k_{1m}^{(n)}x_1) + ik_{1m}^{(n)}Z_{-1}^{(n)}\cos(k_{1m}^{(n)}x_1)/\omega\rho^{p(n)}$ and $k_{1m}^{(n)}$ satisfies the dispersion relation

$$\begin{aligned} & \tan\left(k_{1m}^{(n)} w_1^{(n)}\right) \left(\frac{(\omega \rho^{p(n)})^2}{Z_{-1}^{(n)} Z_1^{(n)}} + \left(k_{1m}^{(n)}\right)^2 \right) \\ & + i k_{1m}^{(n)} \left(\frac{1}{Z_1^{(n)}} + \frac{1}{Z_{-1}^{(n)}} \right) \omega \rho^{p(n)} = 0. \end{aligned} \quad (\text{B3})$$

This last equation is also solved by use of a Muller's algorithm initiated with the low frequency approximations. These modes are again bi-orthogonal and the bi-orthogonality relation reads as²⁸

$$\begin{aligned} & \int_0^{w_1} \Phi_{1m}^{(n)}(x_1) \Phi_{1M}^{(n)}(x_1) dx_1 \\ & = \delta_{Mm} w_1^{(n)} \left(\frac{1}{2} \left(1 - \text{sinc}\left(2k_{1m}^{(n)} w_1^{(n)}\right) \right) - \frac{1}{2} \left(\frac{k_{1m}^{(n)} Z_{-1}^{(n)}}{\omega \rho^{p(n)}} \right)^2 \right. \\ & \quad \times \left(1 + \text{sinc}\left(2k_{1m}^{(n)} w_1^{(n)}\right) \right) + \frac{i Z_{-1}^{(n)}}{w_1^{(n)} \omega \rho^{p(n)}} \\ & \quad \left. \times \left(\sin\left(k_{1m}^{(n)} w_1^{(n)}\right) \right)^2 \right) = \delta_{Mm} w_1^{(n)} N_{1m}^{(n)}. \end{aligned} \quad (\text{B4})$$

APPENDIX C: EXPRESSION OF $I_{mq}^{(n)\pm}$

The terms $I_{mq}^{(n)\pm}$ account for the aperture of the pore and are given by

$$\begin{aligned} I_{mq}^{(n)\pm} & = \frac{e^{\pm i k_{1q} (d^{(n)} + (w/2))}}{2} \left[e^{i k_{1m} (w/2)} \text{sinc}\left(\left(k_{1m} \pm k_{1q}\right) \frac{w}{2}\right) \right. \\ & \quad \left. + e^{-i k_{1m} (w/2)} \text{sinc}\left(\left(k_{1m} \mp k_{1q}\right) \frac{w}{2}\right) \right], \end{aligned} \quad (\text{C1})$$

when one impedance condition is applied on the right/top surface of the n th pore and

$$\begin{aligned} I_{mq}^{(n)\pm} & = \frac{e^{\pm i k_{1q} (d^{(n)} - (w/2))}}{2} \left[e^{-i k_{1m} (w/2)} \text{sinc}\left(\left(k_{1m} \pm k_{1q}\right) \frac{w}{2}\right) \right. \\ & \quad \left. + e^{i k_{1m} (w/2)} \text{sinc}\left(\left(k_{1m} \mp k_{1q}\right) \frac{w}{2}\right) \right], \end{aligned} \quad (\text{C2})$$

when one impedance condition is applied on the left/bottom surface of the n th pore and

$$\begin{aligned} I_{mq}^{(n)\pm} & = \frac{e^{\pm i k_{1q} (d^{(n)} + (w/2))}}{2} \left[e^{i k_{1m} (w/2)} \text{sinc}\left(\left(k_{1m} \pm k_{1q}\right) \frac{w}{2}\right) \right. \\ & \quad \times \left(\frac{i k_m Z_{-}^{(n)}}{\omega \rho^{p(n)}} - i \right) + e^{-i k_{1m} (w/2)} \\ & \quad \left. \times \text{sinc}\left(\left(k_{1m} \mp k_{1q}\right) \frac{w}{2}\right) \left(\frac{i k_m Z_{-}^{(n)}}{\omega \rho^{p(n)}} + i \right) \right], \end{aligned} \quad (\text{C3})$$

when an impedance condition is applied on two opposite surfaces.

¹J.-F. Allard and N. Atalla, *Propagation of Sound in Porous Media*, 2nd ed. (John Wiley & Sons, Ltd., Chichester, UK, 2009), pp. 1–351.

- ²L. De Ryck, Z. Fellah, J.-P. Groby, P. Leclaire, W. Lauriks, A. Wirgin, and C. Depollier, "Acoustic wave propagation and internal fields in macroscopically-inhomogeneous rigid frame porous materials," *J. Appl. Phys.* **102**, 024910 (2007).
- ³D.-Y. Maa, "Potential of microperforated panel absorber," *J. Acoust. Soc. Am.* **104**, 2861–2866 (1998).
- ⁴D.-Y. Maa, "Practical single MPP absorber," *Int. J. Acoust. Vib.* **12**, 3–6 (2007).
- ⁵T. Cox and P. D'Antonio, *Acoustic Absorbers and Diffusers: Theory, Design and Application*, 2nd ed. (Taylor & Francis, Abingdon, UK, 2009), pp. 1–438.
- ⁶X. Olyny and C. Boutin, "Acoustic wave propagation in double porosity media," *J. Acoust. Soc. Am.* **114**, 73–84 (2003).
- ⁷J. Groby, A. Duclos, O. Dazel, L. Boeckx, and W. Lauriks, "Absorption of a rigid frame porous layer with periodic circular inclusions backed by a periodic grating," *J. Acoust. Soc. Am.* **129**, 3035–3046 (2011).
- ⁸C. Lagarrigue, J.-P. Groby, V. Tournat, O. Dazel, and O. Umnova, "Absorption of sound by porous layers with embedded periodic array of resonant inclusions," *J. Acoust. Soc. Am.* **134**, 4670–4680 (2013).
- ⁹C. Boutin, "Acoustics of porous media with inner resonators," *J. Acoust. Soc. Am.* **134**, 4717–4729 (2013).
- ¹⁰J. Groby, B. Nennig, C. Lagarrigue, B. Brouard, O. Dazel, and V. Tournat, "Enhancing the absorption properties of acoustic porous plates by periodically embedding Helmholtz resonators," *J. Acoust. Soc. Am.* **137**, 273–280 (2015).
- ¹¹T. Dupont, P. Leclaire, O. Sicot, X. Gong, and R. Panneton, "Acoustic properties of air-saturated porous materials containing dead-end porosity," *J. Appl. Phys.* **110**, 094903 (2011).
- ¹²P. Leclaire, O. Umnova, T. Dupont, and R. Panneton, "Acoustical properties of air-saturated porous material with periodically distributed dead-end pores," *J. Acoust. Soc. Am.* **137**, 1772–1782 (2015).
- ¹³Z. Yang, J. Mei, M. Yang, N. Chan, and P. Sheng, "Membrane-type acoustic metamaterial with negative dynamic mass," *Phys. Rev. Lett.* **101**, 204301 (2008).
- ¹⁴J. Mei, G. Ma, M. Yang, Z. Yang, W. Wen, and P. Sheng, "Dark acoustic metamaterials as super absorbers for low-frequency sound," *Nature Commun.* **3**, 756 (2012).
- ¹⁵V. Romero-Garcia, G. Theocharis, O. Richoux, A. Merkel, V. Tournat, and V. Pagneux, "Perfect and broadband acoustic absorption by critically coupled sub-wavelength resonators," *Sci. Rep.* **6**, 19519 (2016).
- ¹⁶A. Merkel, G. Theocharis, O. Richoux, V. Romero-Garcia, and V. Pagneux, "Control of perfect absorption in 1D scattering: An acoustic example," in *Proceedings of Phononics 2015* (2015), pp. 390–391.
- ¹⁷J. Groby, A. Lardeau, W. Huang, and Y. Aurégan, "The use of slow sound to design simple sound absorbing materials," *J. Appl. Phys.* **117**, 124903 (2015).
- ¹⁸G. Ma, M. Yang, S. Xiao, Z. Yang, and P. Sheng, "Acoustic metasurface with hybrid resonances," *Nature Mater.* **13**, 873–878 (2014).
- ¹⁹A. Santillan and S. Bozhevolnyi, "Demonstration of slow sound propagation and acoustic transparency with a series of detuned resonators," *Phys. Rev. B* **89**, 184301 (2014).
- ²⁰G. Yu and X. Wang, "Acoustical 'transparency' induced by local resonance in Bragg bandgaps," *J. Appl. Phys.* **115**, 044913 (2014).
- ²¹A. Cicek, O. Kaya, M. Yilmaz, and B. Ulug, "Slow sound propagation in a sonic crystal linear waveguide," *J. Appl. Phys.* **111**, 013522 (2012).
- ²²Y. Aurégan, L. Xiong, and W. Bi, "Acoustical behavior of purely reacting liners," in *Proceedings of the 19th AIAA/CEAS Aeroacoustics Conference*, American Institute of Aeronautics and Astronautics, Inc., Berlin (2013), pp. 1–8.
- ²³G. Theocharis, O. Richoux, V. R. García, A. Merkel, and V. Tournat, "Limits of slow sound propagation and transparency in lossy, locally resonant periodic structures," *New J. Phys.* **16**, 093017 (2014).
- ²⁴W. Robertson, C. Baker, and C. B. Bennet, "Slow group velocity propagation of sound via defect coupling in a one-dimensional acoustic band gap array," *Am. J. Phys.* **72**, 255–257 (2003).
- ²⁵Y. Xie, A. Konneker, B.-P. Popa, and S. Cummer, "Tapered labyrinthine acoustic metamaterials for broadband impedance matching," *Appl. Phys. Lett.* **103**, 201906 (2013).
- ²⁶A. Santillan and S. Bozhevolnyi, "Acoustic transparency and slow sound using detuned acoustic resonators," *Phys. Rev. B* **84**, 064304 (2011).
- ²⁷E. Redon, A.-S. Bonnet-Ben Dhia, J.-F. Mercier, and S. Poernomo Sari, "Non-reflecting boundary conditions for acoustic propagation in ducts with acoustic treatment and mean flow," *Int. J. Numer. Meth. Eng.* **86**, 1360–1378 (2011).

- ²⁸J. B. Lawrie and I. Abrahams, "An orthogonality relation for a class of problems with high-order boundary conditions; applications in sound-structure interaction," *Q. J. Mech. Appl. Math.* **52**, 161–181 (1999).
- ²⁹A. Bensoussan, J. Lions, and G. Papanicolaou, *Asymptotic Analysis for Periodic Structures* (North-Holland, Amsterdam, The Netherlands, 1978), pp. 1–387.
- ³⁰A. Wood, *A Textbook of Sound* (G. Bell and Sons Ltd., London, UK, 1932), pp. 1–593.
- ³¹A. Morel, S. Felix, and J.-F. Mercier, "Enhanced transmission through gratings: Structural and geometrical effects," *Phys. Rev. B* **88**, 115416 (2013).
- ³²N. Fang, D. Xi, J. Xu, M. Ambati, W. Srituravanich, C. Sun, and X. Zhang, "Ultrasonic metamaterials with negative modulus," *Nature Mater.* **5**, 452–456 (2006).
- ³³N. Nematı and D. Lafarge, "Check on a nonlocal Maxwellian theory of sound propagation in fluid-saturated rigid-framed porous media," *Wave Motion* **51**, 716–728 (2014).
- ³⁴T. Luk, S. Campione, I. Kim, S. Feng, Y. Jun, S. Liu, J. Wright, I. Brener, P. Catrysse, S. Fan, and M. Sinclair, "Directional perfect absorption using deep subwavelength low-permittivity films," *Phys. Rev. B* **90**, 085411 (2014).
- ³⁵F.-P. Mechel, *Formulas of Acoustics*, 2nd ed. (Springer-Verlag, Berlin, Heidelberg, 2008), pp. 316–327.
- ³⁶P. Drude, "Transparent isotropic media," *Wied. Ann* **43**, 146 (1891).
- ³⁷C. Simovski, "On electromagnetic characterization and homogenization of nanostructured metamaterials," *J. Opt.* **13**, 013001 (2011).
- ³⁸X. Cai, Q. Guo, G. Hu, and J. Yang, "Ultrathin low-frequency sound absorbing panels based on coplanar spiral tubes or coplanar Helmholtz resonators," *Appl. Phys. Lett.* **105**, 121901 (2014).
- ³⁹J. Groby, W. Lauriks, and T. Vigran, "Total absorption peak by use of a rigid frame porous layer backed with a rigid multi-irregularities grating," *J. Acoust. Soc. Am.* **127**, 2865–2874 (2010).
- ⁴⁰M. Stinson, "The propagation of plane sound waves in narrow and wide circular tubes, and generalization to uniform tubes of arbitrary cross-sectional shape," *J. Acoust. Soc. Am.* **89**, 550–558 (1991).